ADVANCED MATERIALS INTERFACES
Open Access
www.advmatinterfaces.de

Influence of Heat Treatments on the Photocatalytic Activity of TiO_2 Surfaces Produced by Direct Laser Interference Patterning

Tobias Fox, Fabian Kay Bonner, Christoph Pauly, Guido Kickelbick, and Frank Mücklich*

Direct laser interference patterning (DLIP) has in previous work shown to be an effective tool for producing photocatalytic surfaces in a single relatively simple processing step. These surfaces can be interesting candidates for antifouling or self-cleaning surfaces, as well as substrates for photocatalytic water treatment. In this contribution, various heat treatments are performed both during and after the laser processing to create surfaces with even higher photocatalytic activities and to better understand the formation of various process oxides and their effect on the resulting activity. The photocatalytic activity of the samples is measured by methylene blue degradation and correlated to their chemical composition and morphology. Furthermore, a small prototype is built using low-cost materials to prove the scalability of the approach.

1. Introduction

Producing photocatalytic surfaces based on titanium and its oxides generally requires multi-step processes that require nanoparticle synthesis or wet chemical processing.[1–5] To facilitate the large-scale production of active surfaces, alternative processing routes like laser oxidation are becoming more prevalent.[6–12]

In previous work, it was shown that Direct Laser Interference Pattering (DLIP) can be used to produce photocatalytic surfaces in a single processing step through the creation of a suitable topography as well as the creation of photocatalytically active titanium oxides.[13] However, it was hypothesized that the activity of these surfaces is diminished by a metastable TiO phase that forms during the pattering as well as possibly vast amounts of amorphous titanium oxides, both of which could potentially be removed via thermal activation. However, suitable heat treatment should not achieve temperatures high enough to transform the photocatalytically active, metastable TiO_2 anatase phase in its less active rutile configuration. This study therefore investigates the effects of different heat treatments during and after the laser process on the oxide chemistry and morphology as well as the resulting photocatalytic activity. These treatments aim to increase the activity of the surfaces as they allow the aforementioned more metastable phases to relax into more stable TiO_2 phases like rutile and anatase. Doing so could ideally increase the amount of anatase rutile heterojunctions, which would most likely have additional beneficial effects on the photocatalytic activity.[14–17]

Additionally, a prototype employing a patterned area of 80–200 mm and 1.5 L of methylene blue solution was built using easily available, low-cost materials to gain first insights regarding the scalability of the approach.

2. Results and Discussion

2.1. Surface Topography

Samples with periodic surface structures fabricated by DLIP can express hierarchical surface structures consisting of the actual DLIP pattern and a sub-structure. These sub-structures can be laser-induced periodic surface structures (LIPSS), remnants from the ablation process, or structures originating from the redeposition of material.[13,18–21] As expected from the results of previous work, the surfaces depicted in **Figure 1** show a hierarchical structure where the material is ablated from the regions with maximal laser intensity, and a part of this material is then redeposited as oxide at the intensity minima of the applied interference pattern. This oxide layer has a porous substructure that depends on the pulse energy. For low pulse energies (L-samples) only small amounts of material are ablated per pulse. The ablated material then has time to oxidize and agglomerate at the interference minima. This leads to the formation of a complex, open-pored oxide structure at those locations (Figure 1a,c). High pulse

T. Fox, F. K. Bonner, C. Pauly, G. Kickelbick, F. Mücklich
Functional Materials
Saarland University
66123 Saarbrücken, Germany
E-mail: tobias.fox@uni-saarland.de
T. Fox, F. K. Bonner, C. Pauly, G. Kickelbick, F. Mücklich
Inorganic Solid-State Chemistry
Saarland University
Campus, Building C4 1, 66123 Saarbrücken, Germany

The ORCID identification number(s) for the author(s) of this article can be found under https://doi.org/10.1002/admi.202400786

DOI: 10.1002/admi.202400786

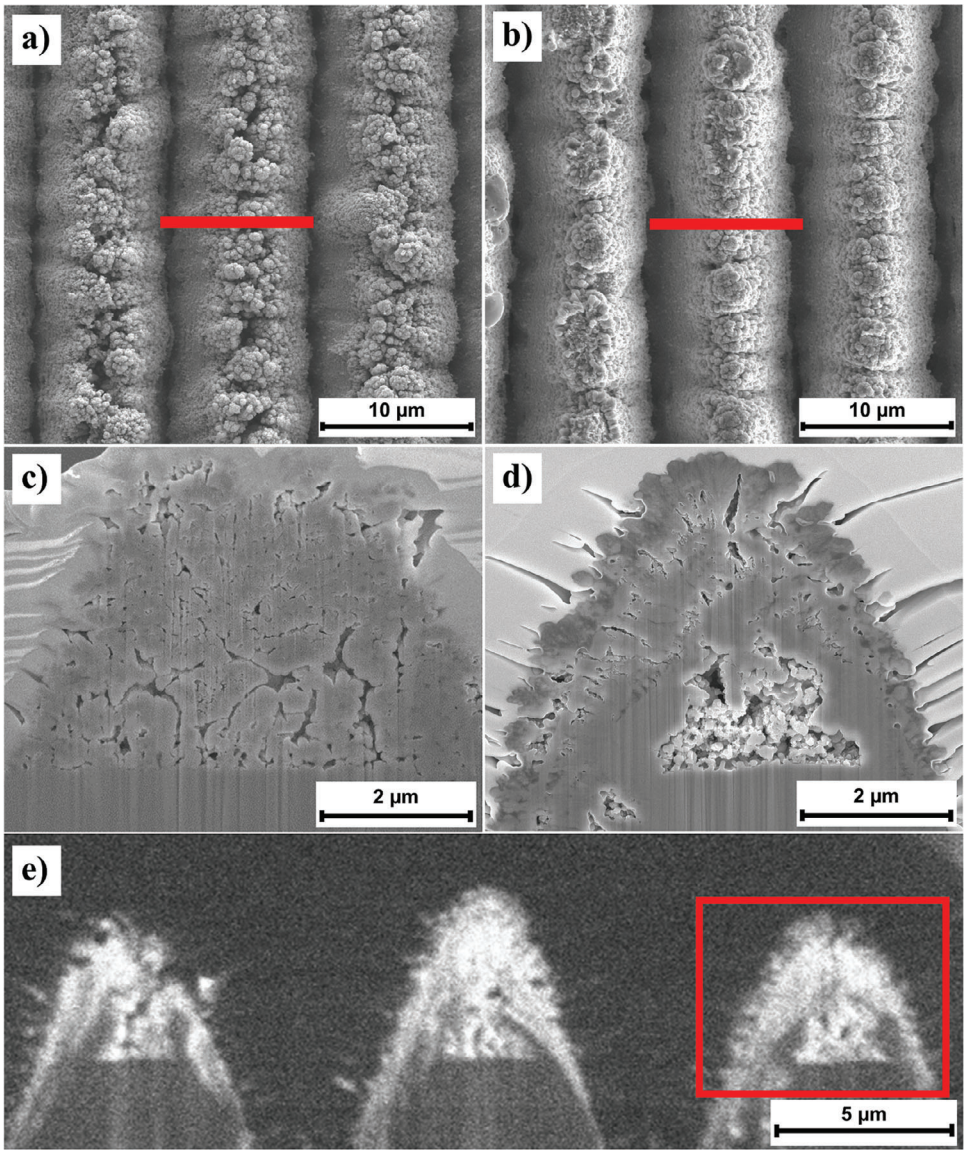

Figure 1. SEM images of surfaces produced at room temperature with a) low and b) high pulse energies together with close-ups of respective cross sections (c/d). e) Chemical contrast between titanium and oxide can be achieved by the secondary ion contrast using Xenon ions. The red markings in (a,b) indicate the approximate location of the respective cuts, whereas the red rectangle in e indicates the area depicted in (d).

energies (H-samples), on the other hand, produce molten material that forms a cone-shape on top of the maxima that is then covered with oxide (Figure 1b,d). Secondary ion imaging of the focused ion beam (FIB) cross-sections is applied and yields superior contrast between metal and oxide. The convolved mixture of metal and metal oxide on H-samples becomes visible (Figure 1e). The result of this formation process is a surface that rather shows large pores within the structure instead of an open "coral-like" oxide structure. In addition to this oxide structure, the surfaces produced at elevated temperatures show an extremely fine oxidic structure on top, as can be shown in **Figure 2** depicting a sample produced with high pulse energy at 400 °C. The heat treatments after the patterning, on the other hand, had no visible effect on the observed porosity as the treatment temperature and time apparently were not sufficient to cause significant densification.

2.2. Surface Chemistry

This section discusses the surface chemistry of the produced samples on the basis of X-ray diffraction (XRD) measurements. While respective measurements were performed for all samples, the observed trends are discussed using the most relevant diffractograms shown in **Figure 3**. These have been analyzed using Rietveld refinement to determine the relative phase concentrations that are presented in **Table 1**.

Generally speaking, a high anatase content is desirable as anatase is seen as the most photocatalytically active phase. A combination of anatase with rutile can further increase the activity as the combination of both phases facilitates charge separation and prevents recombination.[14,22,23] The oxygen-deficient phases hongquite and tistarite (TiO and Ti_2O_3) have in former

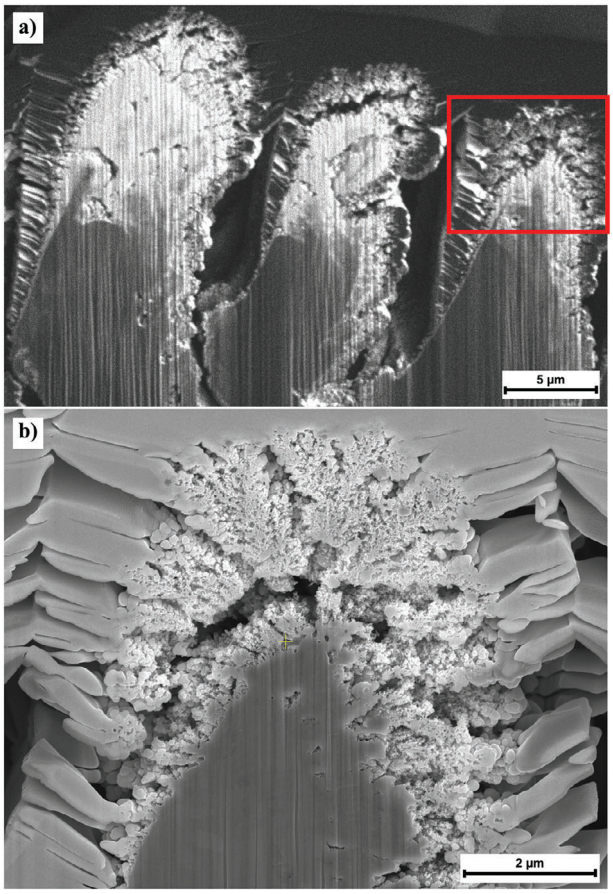

Figure 2. Sample surfaces patterned at 400 °C with high pulse energies showing vast amounts of oxide in the ion contrast overview a) and a very fine, porous oxide structure in the magnified SE image b) of the rightmost peak.

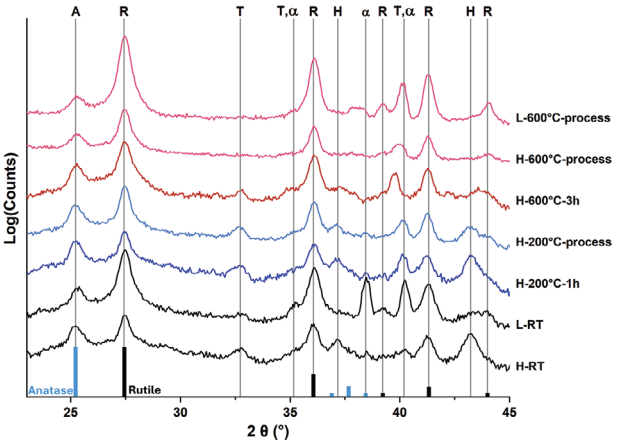

Figure 3. Exemplary XRD curves for samples with high (H) and low (L) pulse energies and different heat treatment temperatures and times. The observed peaks are indicated using the PDF files listed in Section 3.3.2 and labeled with the respective phases. A: Anatase; R: Rutile; α: α-Titanium; T: Tistarite (Ti_2O_3); H: Hongquite (TiO). At the bottom of the graph, the reference spectra for rutile and anatase are plotted with their respective intensities according to the PDF cards listed in the methods section.

work shown to have a mostly negative impact on the photocatalytic activity.[13]

Although all samples were exposed to the same accumulated fluence it can be shown in Figure 3 and Table 1 that even the samples produced at room temperature show a significant difference in oxide composition depending on the applied pulse energy. While both sample sets show rutile and anatase the samples produced with high pulse energy show significantly more oxygen-deficient oxides TiO and Ti_2O_3. This observation is in agreement with former work[13] and likely stems from the fact that more titanium is ablated per pulse at high pulse energies. As a result, the oxygen content in the resulting plasma is not sufficient to fully oxidize the material. It is additionally observed that for lower pulse energies the diffractograms show pronounced peaks of alpha titanium. However, as it was seen by scanning electron microscopy (SEM) that the surface of the peaks is covered in oxides, it is suggested that the lower pulse energies produce less oxide in the topographic troughs while the higher pulse energies produce a thin oxide layer even in these valleys. For the samples exposed to higher temperatures, a shift of the α-Ti reflections toward lower angles can be observed. This shift can be explained by the incorporation of oxygen into the titanium lattice, whichaffects the lattice constant and the c/a ratio.[24,25]

Simultaneously the oxygen-deficient phases hongquite and tistarite (TiO and Ti_2O_3) partially disappear during the heat treatments. Especially the hongquite signal that was relatively strong at room temperature (H-RT in Figure 3) is greatly reduced when the sample is patterned at 200 °C. This reduction in signal implies that the heat treatment halved the amount of TiO from 22 mass% for the room temperature sample to 11 mass% for the sample patterned at 200 °C. For both laser treatments at 600 °C

Table 1. Phase concentrations in mass% determined from the XRD measurements shown in Figure 3 via Rietveld refinement. The error of the measurement is 1 mass% for all measurements.

Sample	TiO_2 [rutile]	TiO_2 [anatase]	Ti_2O_3 [tistarite]	TiO [hongquite]	alpha-Ti
L-RT	79	14	0	4	3
H-RT	49	20	8	22	1
H-200°−1 h	47	23	10	18	2
H-200°-process	55	23	9	11	2
H-600°−3 h	66	21	3	8	2
H-600°-process	77	19	0	2	3
L-600°-process	88	7	0	2	2

hongquite is barely visible. Tistarite behaves similarly, although in contrast to honquite some amount of tistarite appears to be remaining in the sample heat treated at 600 °C after the patterning.

When regarding the left side of the diffractograms, the anatase and rutile peaks can clearly be distinguished. For the room temperature samples, the area below the peaks also indicates the presence of a significant amount of amorphous phase as is to be expected with regard to the high cooling rates that result during the redeposition process. Anatase has a higher Gibbs energy than rutile at all temperatures and therefore generally exists as a metastable phase and will transform into rutile at ≈600 °C although observations vary from 400 to 1200 °C. Anatase is however more stable than rutile at particle sizes below 40 nm as it possesses a smaller surface energy. As a result, the redeposited material that is partially amorphous or has very small grain sizes likely is the main source of anatase on the surface. At elevated temperatures, the amorphous material appears to gradually transform into rutile. Even at 600 °C some anatase still remains both in the sample heated after the laser patterning and the sample that was patterned at 600 °C. Particularly the fact that the sample patterned at 600 °C still shows anatase indicates that very small grains of anatase are formed during the process and did not have the time to grow and transform into rutile.[26–29]

It must be noted though, that the information depth of the XRD measurements is limited to ≈125 nm as a result of the small angle of incidence of 0.8° when assuming the absorption characteristics of rutile. This means that the oxide composition below the surface cannot be assessed by these measurements. The different holding times did not cause visible differences in the resulting spectra for any of the samples, which is why they were not plotted in Figure 3.

2.3. Photocatalytic Activity

Methylene Blue (MB) degradation experiments were performed as described in Section 3.3.3. After the experiment, the remaining concentrations were measured via UV–vis spectroscopy (Section 3.3.4) and compared to the initial concentration C_0 (50 µM). As previous work.[13] could already show stable cycling stability for similar surfaces, this work did not investigate multiple degradation cycles.

Figure 4 depicts the results of the degradation experiments for samples that were heat-treated after the patterning. For two reference measurements, one containing only the methylene blue solution without any sample and one including untreated titanium, the methylene blue concentrations remained unchanged ($C/C_0 = 1$), which is why they were not plotted here. For the two outliers at 200 °C-1h-H and 200 °C-3h-L, it was observed after the experiment that air bubbles had remained at the sample surfaces, which likely resulted in a decreased activity. In a small-scale repetition of the experiment, 200 °C-3h-L showed an activity similar to the other L samples. Overall, it could be observed that all heat treatments improved the activity of the surface and there is no significant difference between different pulse energies. This is consistent with former experiments without heat treatments.[13] It can additionally be observed that all but the 200 °C-1 h treatment resulted in a major increase in photocatalytic activity. This increased performance can likely be attributed to an increase in

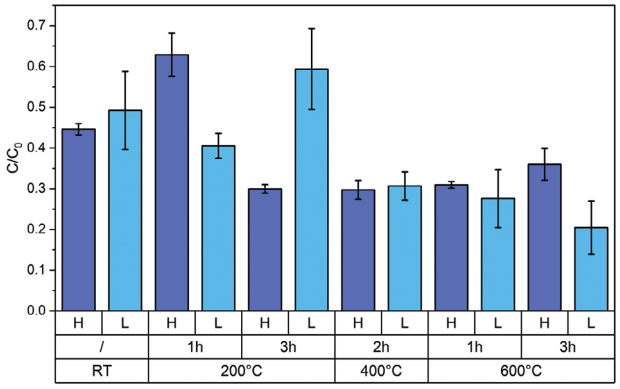

Figure 4. Remaining MB concentrations as measured by UV–vis spectroscopy. The methylene blue concentration after the experiment was divided by the initial concentration C_0 to determine a percentual decrease for various heat-treated samples and the laser patterned reference that remained at room temperature (RT). H and L indicate high and low pulse energies.

crystallinity as amorphous oxides crystallize and the peak for rutile becomes more pronounced.[30] Even though the pulse energy influences both the surface topography and chemistry (mainly by producing more TiO at higher pulse energies), it tends to have only a small impact on the photocatalytic activity. This is especially true after the heat treatment where the oxygen-deficient phases crystallize to form rutile. Overall, this crystallization can be assumed to be the main cause of the increase in activity for the heat-treated samples as the presence of oxygen-deficient phases has in a former study shown to decrease the activity of the surface.[13]

The results of the experiments employing the heat treatment during the patterning process are shown in **Figure 5**. To assess the effect of the heat treatment in air without patterning, an unpatterned reference was produced for each temperature. Especially the reference at 400 °C showed a minor photocatalytic activity that is consistent with the results of a former study that observed a mixture of anatase and rutile in samples produced at 450 °C.[31] As these results show, an increase in temperature to

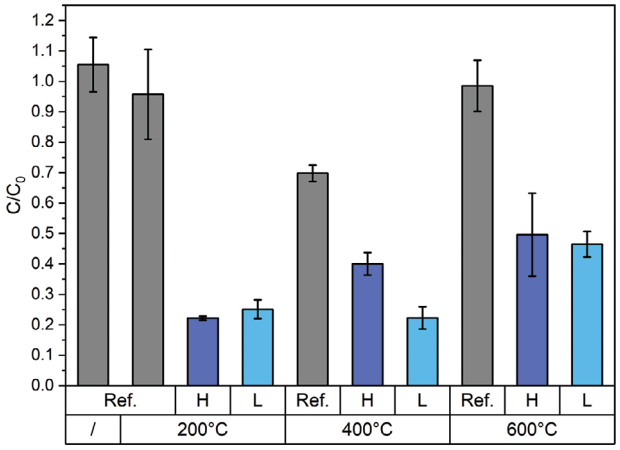

Figure 5. MB degradation caused by samples that were patterned at elevated temperatures.

Table 2. Kinetic constants for all patterned samples.

Processing temperature [°C]	Heat-treatment temperature [°C]	Heat-treatment time [h]	Pulse energy	Kinetic constant [1/h]
RT	200	1	H	0.23 ± 0.04
			L	0.45 ± 0.04
		3	H	0.60 ± 0.02
			L	0.27 ± 0.09
	400	2	H	0.61 ± 0.04
			L	0.59 ± 0.06
	600	1	H	0.59 ± 0.01
			L	0.66 ± 0.12
		3	H	0.51 ± 0.02
			L	0.83 ± 0.09
	–		H	0.40 ± 0.02
			L	0.36 ± 0.09
200	–		H	0.75 ± 0.01
			L	0.69 ± 0.06
400	–		H	0.46 ± 0.05
			L	0.76 ± 0.08
600	–		H	0.37 ± 0.13
			L	0.38 ± 0.04

only 200 °C during the laser patterning was enough to achieve very high activities. In fact, the first-order kinetic constant of the sample produced with a high pulse energy at 200 °C is with 0.75 1/h one of the three highest of the whole study, as can be seen in **Table 2**. This correlates well with the observed anatase content of 23% (Table 1), which was one of the highest observed in this study.

As mentioned above, the increase in photocatalytic activity is most likely a result of increased crystallinity and a lower content of TiO. As amorphous TiO_2 is generally considered inactive, its presence can reduce the activity of the surface, and its crystallization into anatase is very beneficial. However, rutile is thermodynamically more stable than anatase except for nanostructured grains (<40 nm) where anatase's smaller surface energy stabilizes the phase.[26–28,32] As a result, an effective heat treatment needs to deliver sufficient activation energy for the nucleation of amorphous TiO_2 and the transformation of TiO into pure Ti and TiO_2 without resulting in crystal growth and the formation of rutile.

Additional synergistic effects can be expected if anatase and either rutile or Ti_2O_3 are present in the surface, and if an electrically conductive connection (heterojunction) between those phases exists. This is because such heterojunctions can facilitate charge separation and thereby decrease the probability that charge carriers recombine right after their formation.[32–39]

As some of the heat treatments performed in this work resulted in major increases in photocatalytic activity without a vast increase in anatase content (Figure 3), it can be assumed that the increase in activity is a result of an increased charge carrier mobility and the formation of heterojunctions. To validate this hypothesis, Transmission Electron Microscopy (TEM) analysis was attempted. However, as a result of the complex surface topography, the preparation of sufficiently thin TEM lamella without the loss of the porous surface oxides still proved challenging by the time of publication. Future research will follow up on this question.

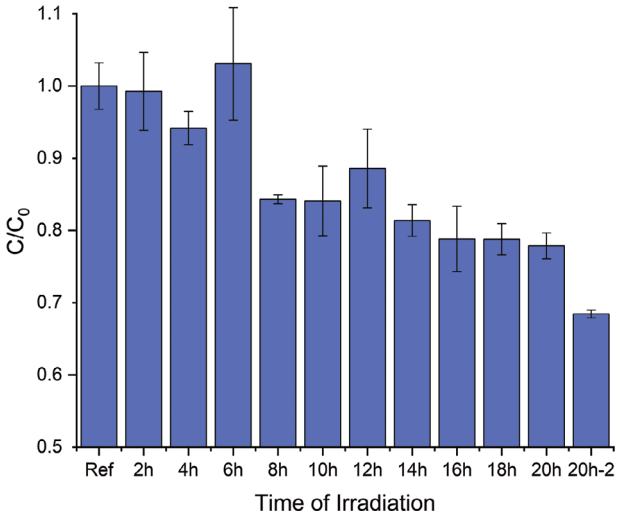

Figure 6. Methylene blue degradation achieved by the prototype. The measurement labeled as 20h-2 was performed after the evaporation of 200 mL was compensated.

2.4. Upscaling of the Approach

In order to gain insights regarding the scalability of the approach, laser patterning was performed on an 80 × 200 mm area and tested with 1.5 liters of methylene blue solution using a 30 W UV lamp. The setup is explained in greater detail in Section 3.4.

Samples of the methylene blue solution were retrieved in intervals of 2 h of UV irradiation. By the end of the experiment, 200 mL of water had evaporated and were replaced. Therefore, two data points exist for 20 h of irradiation, one before and one after the evaporation was compensated. The resulting degradation is shown in **Figure 6**. It can be seen that the concentration is continuously reduced with increasing irradiation time. After evaporation was compensated by adding water it was revealed that the concentration of the methylene blue solution had been reduced by ≈30%.

To try and compare the performance of the prototype with that of the lab setup the number of degraded molecules per hour, watt, and cm^2 was calculated for both setups using the k values of the RT-H sample from Table 2 and the 20h-2 sample from Figure 6. Although the setups are vastly different, one employing a mirrored chamber and UV lamps, the other using an LED source and a vastly different scale, accounting for the active surface, exposure time, and UV power should show if both setups achieve comparable degradation rates. The result of this comparison is shown in **Table 3**. The time constant k is much smaller for the prototype than for the lab setup that can be explained by the smaller surface-to-volume fraction of the prototype given the large sample volume of 1.5 L. When comparing the actual normed degradation speeds of both setups it becomes apparent that both achieve similar efficiencies with the prototype having a slightly better

Table 3. Comparing the prototype to the normal lab setup discussed before.

	Lab setup	Prototype
MB Solution [µL]	125	1.5×10^6
Active Area [cm^2]	0.25	160
UV-Power [W]	32	30
k [1/h]	0.4 ± 0.015	0.019 ± 0.002
C_0 [µM]	50 ± 4.37	50 ± 0.93
Amount of MB [nMol]	6.25 ± 0.546	75 000 ± 1.395
Degradation Efficiency $nMol/(cm^2 * W * h)$	0.216 ± 0.019	0.247 ± 0.006

performance. This increased performance can be attributed to the higher efficiency of the employed LED light source for the prototype compared to the efficiency of the lamps employed in the lab setup. Another factor could be the larger overall reduction of methylene blue for the lab setup, whichcould lead to a depletion of MB that results in a smaller degradation speed toward the end of the experiment. This effect could be amplified as the prototype employed a continuous flow of solution that ensured an even distribution of MB over the surface without the formation of diffusion-limited depletion zones.

3. Experimental Section

3.1. Sample Preparation

The titanium samples used in this work were mirror-polished with a multi-step polishing routine described in previous work.[40] Before the laser patterning the samples were cleaned using water and soap.

The pattering was performed with an edgewave px picosecond laser with 532 nm wavelength, a pulse duration of 12 ps, a maximum repetition rate of 100 kHz, and a maximum average power of 10 W. The optical setup used to split the primary beam into multiple sub-beams and then interfere with those beams on the sample surface was described in detail in a former study.[13]

For the patterning, two different pulse energies namely 10 and 30.7 µJ were used. The resulting spot diameters of 94.7 and 113.5 µm resulted in pulse fluences of 0.143 and 0.309 J cm^{-2} respectively. These sample sets were therefore labeled as low pulse energy (L) and high pulse energy (H). The overlap between pulses was varied by employing pulse distances of 0.134 and 0.409 µm. Thereby the total number of pulses on a given point in the surface was set to be 5250 for the low pulse energy and 2475 for the high one. This scanning procedure achieved an accumulated fluence of 750 J cm^{-2} for both sample sets, which was desired to ensure comparability of both sets. The values were calculated using the calculation routine developed in.[40]

3.2. Heat Treatment

The heat treatment after the patterning was conducted in an oven equipped with a vacuum tube (9.0×10^{-5} to 4.6×10^{-5} mbar) to ensure that the existing metastable oxides can relax into more stable phases without the formation of additional oxides. The minimum and maximum temperatures were chosen as 200 and 600 °C and the holding times as 1 and 3 h. Additionally, a center point was chosen at 400 °C and 2 h. The heating and cooling rate was set as 1 °C min^{-1}. The experiment matrix is depicted in **Figure 7**. The maximum temperature of 600 °C was chosen because the literature reports the formation of pure rutile at higher temperatures (e.g., 750 °C by Barbour et al.[1]). In 2016 Wang et al.[31] have shown that a 6 h heat treatment at 450 °C produces a mixture of rutile and anatase in the surface. It should be noted that these studies were performed in oxygen-rich atmospheres. The experiments in this work however aim not to create additional oxide but only to transform existing metastable phases. As these processes were expected to require less diffusion than the formation of a thick oxidic film on the surface, the treatment times were varied on a shorter time scale.

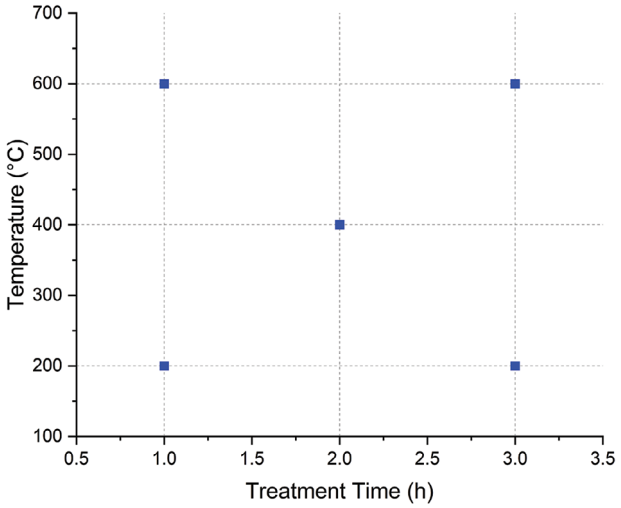

Figure 7. Parameter matrix for the heat treatments after the laser patterning.

For the heat treatment during the patterning, the samples were placed on a heating plate made of stainless steel that was equipped with two 200 W heating elements. The samples were placed on this plate before it was heated with a heating rate of 5 °C min^{-1}. The patterning was started 5 min after the target temperature was reached.

3.3. Surface Analysis

3.3.1. SEM/FIB/EDS

FIB cross-sectioning and SEM imaging were performed using both a Ga-FIB/SEM (FEI Helios Nanolab600) and one employing a xenon ion source (Thermo Fisher Helios G4 PFIB). Secondary electron imaging was done at an acceleration voltage of 5 kV. Secondary ion imaging was done using the xenon ion beam at 30 kV and the proprietary ICE detector.

Table 4. Crystallographic references used for the evaluation of the XRD curves.

Phase	ICDD-Reference Code
α-Titanium (Ti)	00-044-1294
Rutile (TiO_2)	01-079-5858
Anatase (TiO_2)	01-075-2545
Tistarite (Ti_2O_3)	04-005-4652
Hongquiite (TiO)	04-004-2981

3.3.2. X-Ray Diffraction

The grazing incidence XRD measurements were performed using Copper Kα radiation in a diffractometer equipped with a Goebel mirror (PANalytical X'Pert Pro MPD). The 2Theta range was 20°–75° with a step size of 0.05°, an incidence angle of 0.8°, and a dwell time of 35 s per step. For the measurements, the orientation of the pattern was adjusted to be parallel to the incoming beam to minimize shadowing effects. The powder diffraction files that were used for the analysis are given in **Table 4**.

Rietfeld[41,42] refinement was performed using the analysis software TOPAS from Bruker.[43] The respective crystallographic data were sourced from the Pearson-Database.[44]

3.3.3. Methylene Blue Degradation

To quantify the photocatalytic activity of the surfaces, three individual 5 × 5 mm samples for each parameter were placed in glass vials and brought in contact with 125 µL of a 50 µM methylene blue (MB) solution. The vials were then randomly placed in a holder and covered with a UV-transparent PMMA cover to minimize evaporation. The holder was then placed in a commercially available UV source (Naistar NS 01 UK&EU) employing four 8 W fluorescence lamps with a central wavelength of 365 nm. After an irradiation time of 2 h 90 µL of the solution was retrieved to determine the remaining MB concentration via UV–vis spectroscopy. For this, the 90 µL samples were diluted with 160 µL of distilled water to achieve a sample volume of 250 µL.

These samples were placed in a Perkin Elmer Lambda 750 spectrometer where their absorption was measured in a wavelength range from 600 to 700 nm with a 4 nm step size. The optical path of the used cuvette was 10 mm. The concentration was determined by comparing the sample's absorption at 664 nm with a calibration curve. To plot the results the remaining concentration was normalized with the initial concentration. The fraction C/C_0 therefore indicates the amount of MB left in the solution after two h of irradiation. The first-order kinetic constant was calculated using Equation (1):

$$k = \frac{1}{t} \times \ln\left(\frac{C_0}{C}\right) \quad (1)$$

3.4. Preparation of the Prototype

To produce a prototype on a larger scale, a commercially available grade 1 titanium foil with 0.1 mm thickness was bought from Evek GmbH via a German supermarket chain (Kaufland Stiftung & Co. KG). After cleaning with ethanol, the foil was placed in a customized sample holder and laser patterned without any prior surface treatment. To keep it as simple as possible, the patterning was performed at room temperature with the high pulse energy setting. A total area of 200 × 80 mm was patterned.

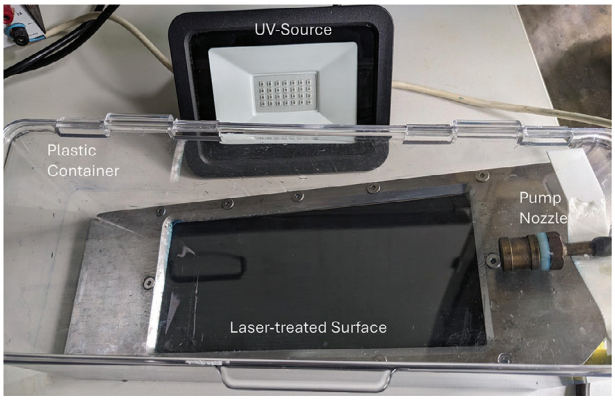

Figure 8. Prototype for the upscaled degradation experiment consisting of a plastic container, a pump, the patterned foil, and a UV source. The methylene blue solution circulated by a small pump located underneath the nozzle on the right and flows over the patterned foil. The UV source in the background is placed on top of the UV-transparent lid of the box.

To remove any loose oxide particles the sample was washed with deionized water and then placed in a polymer container as depicted in **Figure 8**. To circulate the methylene blue solution a small pump was placed under the sample holder and the nozzle was fixed near the top end of the foil. As a UV source, a generic 30 W LED lamp with a center wavelength of 365 nm was bought from Amazon marketplace. To start the experiment 1.5 L of 50 µM methylene blue solution was added, the pump was switched on, the lid of the box was closed, and the UV lamp was placed on the UV-transparent lid.

Before starting both the lamp and the timer, the setup was left to run in the dark for 30 min. Afterward, the first sample was withdrawn to mark the initial concentration. Additional samples were withdrawn every 2 h. Every time, three samples of 90 µL were withdrawn to ensure that the subsequent measurement parameters for the UV–vis were identical to those of the previous measurements. After every withdrawal, the setup was left for several minutes to let the UV lamp cool down. After 20 h of UV exposure, a total of 200 mL of water had evaporated and was replaced after which another sample (20 h-2) was retrieved.

4. Conclusion

It could be shown that heat treatments after and during laser processing can improve the photocatalytic activity of the resulting surfaces. Especially the laser treatment at 200 °C appears to be a feasible approach when producing photocatalytic surfaces at a larger scale without adding a second processing step. It could further be shown that the increase in activity mainly stems from the transition of amorphous and oxygen-deficient phases (especially TiO) into crystalline anatase and rutile phases. It is further hypothesized that a large number of heterojunctions between those phases exist, which could further explain the increase in

reactivity. Finally, one of the patterns was chosen for a larger-scale prototype employing everyday materials. The prototype achieved a degradation efficiency of 0.25 mMol per hour, cm^2, and watt of UV irradiation. Given that this laser treatment can be applied on large surfaces relatively easily, this approach could facilitate wastewater treatment using sunlight and respective photoreactors.

Acknowledgements

The authors gratefully acknowledge funding for the ZuMat project, supported by the State of Saarland from the European Regional Development Fund (Europäischer Fonds für regionale Entwicklung, EFRE). Funding by the German Research Foundation (DFG) for both the PFIB/SEM instrument (INST 256/510-1 FUGG) and the picosecond DLIP machine (INST 256/470-1 FUGG) is greatly acknowledged. Technical assistance for this work was provided by the Service Center X-ray Diffraction, with financial support from Saarland University and the German Science Foundation (project number INST 256/349-1). The authors thank Dr. Oliver Janka for the support in the interpretation of the X-ray diffraction data presented in this paper. Special thanks go to Bruno Alderete for proofreading and providing language corrections.

Conflict of Interest

The authors declare no conflict of interest.

Data Availability Statement

The data that support the findings of this study are available from the corresponding author upon reasonable request.

Keywords

direct laser interference patterning (DLIP), heat treatment, laser surface functionalization, photocatalytic materials, pulsed laser ablation, titanium oxide, water purification

Received: October 1, 2024
Revised: December 19, 2024
Published online: January 9, 2025

[1] T. Křenek, J. Pola, D. Docheva, T. Stich, R. Fajgar, T. Kovářík, M. Pola, J. Martan, D. Moskal, V. Jandová, J. Kupčík, P. Mikysek, *Surf. Interfaces* **2021**, *26*, 101304.
[2] S. Obregón, V. Rodríguez-González, *J. Sol-Gel Sci. Technol.* **2022**, *102*, 125.
[3] X. Lang, S. Gopalan, W. Fu, S. Ramakrishna, *Bull. Chem. Soc. Jpn.* **2020**, *94*, 8.
[4] T. Gupta, J. C. Samriti, J. Prakash, *Mater. Today Chem.* **2021**, *20*, 100428.
[5] S. Dey, S. C. Roy, *Nano Express* **2021**, *2*, 010028.
[6] P. Fathi-Hafshejani, H. Johnson, Z. Ahmadi, M. Roach, N. Shamsaei, M. Mahjouri-Samani, *J. Laser Appl.* **2021**, *33*, 012014.
[7] M. Mahjouri-Samani, P. Fathi-Hafshejani, H. Johnson, Z. Ahmadi, M. Roach, N. Shamsaei, *ACS Omega* **2020**, *5*, 16744.
[8] A. Medvids, P. Onufrijevs, J. Kaupužs, R. Eglitis, J. Padgurskas, A. Zunda, H. Mimura, I. Skadins, S. Varnagiris, *Opt. Laser Technol.* **2021**, *138*, 106898.
[9] L. Grase, P. Onufrijevs, D. Rezevska, K. Racenis, I. Skadins, J. Karosas, P. Gecys, M. Iesalnieks, A. Pludons, J. Kroica, G. Raciukaitis, *Nanomaterials* **2023**, *13*, 2032.
[10] A. Białous, M. Gazda, K. Grochowska, P. Atanasov, A. Dikovska, N. Nedyalkov, J. Reszczyńska, A. Zaleska-Medynska, G.˜liwiński, *Thin Solid Films* **2016**, *601*, 41.
[11] M. Tošić, V. Rajić, D. Pjević, S. Stojadinović, N. Krstulović, S. Dimitrijević-Branković, M. Momčilović, *Photonics* **2024**, *11*, 284.
[12] A. Barylyak, R. Wojnarowska-Nowak, M. Kus-Liśkiewicz, P. Krzemiński, D. Płoch, B. Cieniek, Y. Bobitski, J. Kisała, *Sci. Rep.* **2024**, *14*, 20926.
[13] T. Fox, P. Maria Delfino, F. Cortés, C. Pauly, D. W. Müller, M. Briesenick, G. Kickelbick, F. Mücklich, *ChemNanoMat* **2023**, *9*, 202300314.
[14] J. Low, B. Cheng, J. Yu, *Appl. Surf. Sci.* **2017**, *392*, 658.
[15] T. Kawahara, T. Ozawa, M. Iwasaki, H. Tada, S. Ito, *J. Colloid Interface Sci.* **2003**, *267*, 377.
[16] Y. Gao, J. Zhu, H. An, P. Yan, B. Huang, R. Chen, F. Fan, C. Li, *J. Phys. Chem. Lett.* **2017**, *8*, 1419.
[17] M. Qiao, J. Yan, L. Qu, B. Zhao, J. Yin, T. Cui, L. Jiang, *ACS Appl. Mater. Interfaces.* **2020**, *12*, 41250.
[18] C. Zwahr, A. Welle, T. Weingärtner, C. Heinemann, B. Kruppke, N. Gulow, M. große Holthaus, A. Fabián Lasagni, *Adv. Eng. Mater.* **2019**, *21*, 1900639.
[19] D. W. Müller, T. Fox, P. G. Grützmacher, S. Suarez, *Sci. Rep.* **2020**, *10*, 3647.
[20] C. Schäfer, P. M. Delfino, P. Leonhard-Trautmann, V. Ott, S. Suarez, M. Stüber, F. Mücklich, C. Pauly, *Adv. Eng. Mater.* **2024**, 2400435, https://doi.org/10.1002/adem.202400435.
[21] S. Marie Lößlein, R. Merz, Y. Rodríguez-Martínez, F. Schäfer, P. G. Grützmacher, D. Horwat, M. Kopnarski, F. Mücklich, *J. Colloid Interface Sci.* **2024**, *670*, 658.
[22] M. Gao, L. Zhu, W. L. Ong, J. Wang, G. W. Ho, *Catal. Sci. Technol.* **2015**, *5*, 4703.
[23] S. G. Kumar, K. S. R. K. Rao, *Appl. Surf. Sci.* **2017**, *391*, 124.
[24] S. Andersson, B. Collén, U. Kuylenstierna, A. Magnéli, *Acta Chem. Scand.* **1957**, *11*, 1641.
[25] H. Okamoto, *J. Phase Equilib. Diffus.* **2011**, *32*, 473.
[26] S. J. Smith, R. Stevens, S. Liu, G. Li, A. Navrotsky, J. Boerio-Goates, B. F. Woodfield, *Am. Mineral.* **2009**, *94*, 236.
[27] O. Van Overschelde, G. Guisbiers, M. Wautelet, *J. Phys. Chem. C* **2009**, *113*, 15343.
[28] D. A. H. Hanaor, C. C. Sorrell, *J. Mater. Sci.* **2010**, *46*, 855.
[29] Y. Li, T. Ishigaki, *J. Cryst. Growth* **2002**, *242*, 511.
[30] P. W. Chou, Y. S. Wang, C. C. Lin, Y. J. Chen, C. L. Cheng, M. S. Wong, *Surf. Coat. Technol.* **2009**, *204*, 834.
[31] G. Wang, J. Li, K. Lv, W. Zhang, X. Ding, G. Yang, X. Liu, X. Jiang, *Sci. Rep.* **2016**, *6*, 31769.
[32] V. Etacheri, C. Di Valentin, J. Schneider, D. Bahnemann, S. C. Pillai, *J. Photochem. Photobiol., C* **2015**, *25*, 1.
[33] D. K. Sharma, S. Shukla, K. K. Sharma, V. Kumar, *Mater. Today Proc.* **2020**, *49*, 3028.
[34] A. Das, M. Patra, R. R. Wary, P. Gupta, R. G. Nair, *Conf. Ser.: Mater. Sci. Eng.* **2018**, *377*, 012101.
[35] G. Zerjav, K. Zizek, J. Zavasnik, A. Pintar, *J. Environ. Chem. Eng.* **2022**, *10*, 107722.
[36] H. Liu, W. Yang, Y. Ma, J. Yao, *Appl. Catal., A* **2006**, *299*, 218.
[37] T. Hu, P. Feng, L. Guo, H. Chu, F. Liu, *Nanomaterials* **2023**, *13*, 2125.

[38] S. Mergenbayeva, T. S. Atabaev, S. G. Poulopoulos, *Catalysts* **2021**, *11*, 18.
[39] H. Zhang, B. Zhang, X. Wang, L. Zou, J. You, S. Lin, *Sust. Energy Fuels.* **2024**, *8*, 2357.
[40] T. Fox, F. Mücklich, *Adv. Eng. Mater.* **2022**, *25*, 2201021.
[41] H. M. Rietfeld, *Acta Crystallogr.* **1967**, *22*, 151.
[42] H. M. Rietfeld, *J. Appl. Cryst.* **1969**, *2*, 65.
[43] Topas, Version 5, Bruker AXS Inc, Karlsruhe, Germany **2014**.
[44] P. Villars, K. Cenzual, *Pearson's Crystal Data: Crystal Structure Database for Inorganic Compounds*, ASM International, Materials Park, OH, USA **2023**.